Check for updates

RESEARCH ARTICLE

NANO · MICRO small
www.small-journal.com

Efficient Perovskite Solar Cells Made by Using a Vapor-Assisted Hot Crystallization Method in Air

Lingjie Lv, Chuantian Zuo, Lixiu Zhang, Zuo Xiao,* Qinye Bao, Chenyi Yi, Jingjing Chang, Keyou Yan, Yong Ding, Congcong Wu, Ke Jin, Hua Dong, Di Wei,* and Liming Ding*

Perovskite solar cells (PSCs) achieve remarkable progress in recent years. However, their commercialization remains hindered by conventional fabrication processes that require antisolvent and prolonged annealing, which compromises scalability and cost-effectiveness. In this study, a vapor-assisted hot crystallization method is proposed, in which a vapor atmosphere is applied during the crystallization process to improve quality of perovskite films. The crystallization and annealing process takes less than 3 min, which is much faster than the antisolvent spin-coating method. In addition, the method can be performed in ambient air without using antisolvent. Systematic characterization demonstrates that solvent vapor atmospheres enhance crystallinity, suppress defect formation, and promote denser growth at grain boundaries. Through synergistic modulation of vapor compositions, large-domain, uniform, and pinhole-free perovskite films are obtained. A power conversion efficiency (PCE) of 23.72% is achieved, which is the highest PCE for perovskite solar cells made by using hot-crystallization method.

1. Introduction

Perovskite solar cells (PSCs) have become a prominent photovoltaic technology in recent years. Their core light-absorbing layer comprises organic-inorganic hybrid materials adopting a perovskite crystal structure (e.g., $CH_3NH_3PbI_3$), demonstrating distinct advantages including high light absorption coefficients, adjustable bandgaps, and low-temperature solution processability.[1–5] Significantly, laboratory-scale small-area devices have achieved a certified power conversion efficiency (PCE) exceeding 26%,[6] rivaling crystalline silicon solar cells. The technology also shows compatibility with flexible substrates[7–9] and roll-to-roll (R2R) processing,[10,11] establishing them as leading candidates for next-generation photovoltaic. However, conventional fabrication methods require extended thermal annealing (30–60 min) to simultaneously accomplish solvent evaporation, grain growth, and defect passivation,[12–16] leading to prolonged processing cycles, suboptimal equipment utilization, and elevated energy consumption. Moreover, high-efficiency PSCs typically require fabrication under inert atmospheres or controlled low-humidity conditions, further constraining production scalability and economic viability.[17,18]

In 2015, Nie et al.[19] reported a solution-based hot-casting method that enabling the fabrication of organometallic perovskite films with millimeter-scale continuity and pinhole-free morphology, yielding solar cell efficiencies approaching

L. Lv, C. Zuo, L. Zhang, Z. Xiao
Key Laboratory of Nanosystem and Hierarchical Fabrication (CAS)
National Center for Nanoscience and Technology
Beijing 100190, China
E-mail: zuocht@nanoctr.cn; xiaoz@nanoctr.cn

L. Lv, L. Zhang
University of Chinese Academy of Sciences
Beijing 100049, China

K. Jin, L. Ding
School of Chemical Engineering and Light Industry
Guangdong University of Technology
Guangzhou 510006, China

D. Wei
Beijing Institute of Nanoenergy and Nanosystems
Chinese Academy of Sciences
Beijing 101400, China
E-mail: weidi@binn.cas.cn

The ORCID identification number(s) for the author(s) of this article can be found under https://doi.org/10.1002/smll.202506937

DOI: 10.1002/smll.202506937

Q. Bao
School of Physics and Electronic Science
East China Normal University
Shanghai 200241, China

C. Yi
State Key Laboratory of Power System
Department of Electronic Engineering
Tsinghua University
Beijing 100084, China

J. Chang
School of Microelectronics
Xidian University
Xi'an 710071, China

K. Yan
School of Environment and Energy
South China University of Technology
Guangzhou 510000, China

Y. Ding
School of Renewable Energy
Hohai University
Nanjing 210024, China

 © 2025 Wiley-VCH GmbH

18%. This approach offers three key advantages: antisolvent-free processing, rapid annealing (≈2 min),[20–23] and enhanced crystallinity,[14,24] while maintaining compatibility with flexible substrates and large-area coating technologies.[25–28] In addition, this method showed high humidity tolerance, enabling fabricating perovskite solar cells in air without humidity control.[29] Nevertheless, the current record efficiency for hot-crystallization-derived devices remains 21.5%,[28] markedly lower than the state-of-the-art efficiency of 26.95% achieved by alternative methods, underscoring the need for innovative approaches to close this performance gap.

In this work, we engineered a vapor-assisted hot crystallization method for perovskite film fabrication, exploiting synergistic effect of DMSO (dimethyl sulfoxide), tBP (4-tert-butylpyridine), and PEA (phenylethylamine) vapors to optimize film quality. The effects of solvent vapor composition on morphological and optoelectronic properties were comprehensively analyzed through SEM, XRD, PL, and UV-Vis absorption spectroscopy. Through coordinated modulation of vapor-phase solvents, we obtained perovskite films with large domains, improved uniformity, and dense morphology within a heating time of <3 min. The corresponding perovskite solar cells exhibited a champion efficiency of 23.72% among hot-crystallization-derived devices, surpassing previous records and validating vapor-phase engineering as a promising strategy for scalable photovoltaic manufacturing.

2. Results and Discussion

Figure 1a schematically illustrates the conventional antisolvent spin coating method for perovskite thin-film fabrication. During the phase transition from precursor solution to perovskite solid-state phase, metastable intermediate phases commonly emerge,[30] necessitating antisolvent intervention to control crystallization kinetics. Post-deposition thermal annealing (≥30 min) is subsequently required to enhance crystallinity and remove residual solvents. Additionally, this method exhibits inherent limitations for large-area film production. Figure 1b demonstrates the vapor-assisted hot crystallization method, where precursor ink is deposited on a preheated substrate (60 °C) via self-spreading[31–33] and transferred to a 150 °C hot plate after complete spreading. A precisely controlled vapor atmosphere is generated by simultaneous evaporation of DMSO, tBP, and PEA at optimized ratios (Figure S1, Supporting Information). Following complete crystallization, the film undergoes brief thermal treatment at 100 °C for only 2 min, reducing annealing time by over 90% compared to conventional methods. Figure 1c elucidates vapor-modulated solvent dynamics during crystallization. Under ambient conditions, direct DMSO evaporation dominates under ambient conditions. In the vapor-assisted crystallization method, vapor-phase DMSO experiences re-incorporation, establishing vapor-liquid equilibrium that delays nucleation and crystal growth. This crystallization retardation mechanism is further analyzed through LaMer diagram analysis of nucleation/growth transitions (Figure 1d). Perovskite solution crystallized directly in air reaches its critical concentration very rapidly (t_1-t_2). This leads to fast nucleation and growth rates (t_2-t_3), resulting in the formation of numerous smaller crystals. In contrast, employing a DMSO vapor during film fabrication can slow down solvent evaporation and reduce supersaturation. This significantly reduces the nucleation rate, allowing fewer nuclei to grow into larger grains, thus forming films with better crystalline quality. Figure 1e,f contrast crystallization processes with and without vapor assistance. The vapor-free process achieves ultrafast crystallization within 6 s but yields films with restricted domain sizes due to kinetic constraints (Figure 1e). Conversely, vapor-assisted crystallization extends the process to 30 s, enabling progressive domain growth and ultimately producing domains with several-fold increased average domain size (Figure 1f).

The SEM images of perovskite films fabricated under different conditions (**Figure** 2a–d; Figure S2, Supporting Information) reveal distinct morphological evolution. The film derived from pure $FAPbI_3$ precursor (without additive or vapor) displays substantial secondary phases (primarily residual PbI_2) (Figure S2a, Supporting Information), whereas films processed with MACl and PbI_2 additives exhibit uniform grain growth and suppressed secondary phase formation (Figure 2a; Figure S2b, Supporting Information). Compared to vapor-free processed counterparts, vapor-assisted films demonstrate enlarged grains, densified grain boundaries, and reduced non-perovskite phase (Figure 2b–d; Figure S2c,d, Supporting Information). Optical microscopic images (Figure 2e–k; Figure S3, Supporting Information) further identify unique leaf-like growth patterns radiating from domain centers in multicomponent perovskite films. Figure 2e–g presents optical microscopy transmission images of perovskite crystallization processes in different vapor. The images reveal that films formed without vapor assistance exhibit smaller grains with disordered grain boundaries (Figure 2e), while those processed under DMSO vapor show larger grains with more regular growth patterns (Figure 2f). Notably, the synergistic effect of the mixed vapor atmosphere further enhances crystallite dimensions and promotes denser growth at grain boundaries, accompanied by significantly reduced light transmittance (Figure 2g). Transmission microscopy analysis indicates that pure $FAPbI_3$ films exhibit the strongest light transmittance and weakest light absorption capacity (Figure S3a,e, Supporting Information). High GB transparency signifies incomplete coverage, enabling shunting pathways and non-radiative recombination. Films prepared without vapor assistance show enhanced light transmission at grain boundaries with inferior light absorption (Figure S3b,f, Supporting Information), while DMSO vapor treatment moderately reduces grain boundary transparency (Figure S3c,d, Supporting Information). Notably, films fabricated under mixed vapor atmosphere present homogeneous surfaces with nearly opaque grain boundaries (Figure S3i–l, Supporting Information). Reflection microscopy reveals that vapor-free processed films contain amorphous distributions at grain

C. Wu
School of Material Science and Engineering
Hubei University
Wuhan 430062, China
H. Dong
School of Electronic Science and Engineering
Xi'an Jiaotong University
Xi'an 710049, China

© 2025 Wiley-VCH GmbH

16136829, 2025, 36, Downloaded from https://onlinelibrary.wiley.com/doi/10.1002/smll.202506937 by Cas-Beijing Institution Of, Wiley Online Library on [29/09/2025]. See the Terms and Conditions (https://onlinelibrary.wiley.com/terms-and-conditions) on Wiley Online Library for rules of use; OA articles are governed by the applicable Creative Commons License

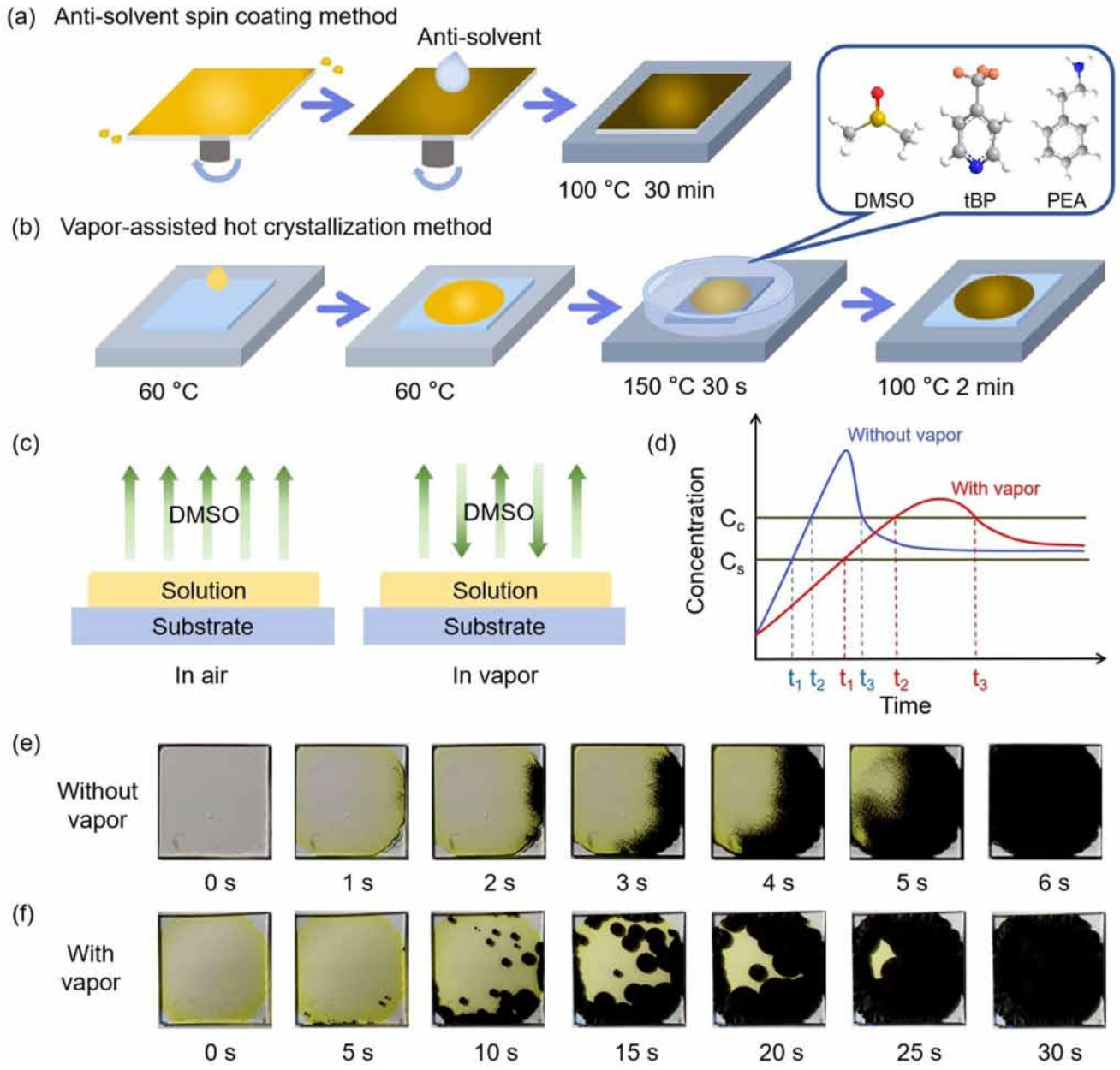

Figure 1. a) Preparation process of perovskite film using antisolvent spin-coating method; b) Preparation process of perovskite film using vapor-assisted hot crystallization method; c) Schematic diagram of solvent vapor movement around the films prepared in ambient air and DMSO vapor; d) LaMer diagram for crystallization process of perovskite solutions in air and DMSO vapor (t_1-t_2: solution, t_2-t_3: nucleation and growth, t_3-t: growth); e) Photograph for the crystallization process of perovskite film fabricated in ambient air; f) Photograph for the crystallization process of perovskite film fabricated via vapor-assisted hot crystallization method.

boundaries, characterized by small domains with wide inter-domain gaps that induce strong light scattering (Figure 2h; Figure S3f, Supporting Information). DMSO vapor-treated samples exhibit substantially enlarged domain sizes with narrowed gaps (Figure 2i; Figure S3g,h, Supporting Information). Most remarkably, films processed in a mixed vapor atmosphere containing DMSO, tBP, and PEA in optimized ratios demonstrate densely packed grain boundaries with minimized defects, achieving superior structural integrity (Figure 2j,k; Figure S3m–p, Supporting Information).

XRD analysis of compositionally varied perovskite films (Figure S4a, Supporting Information) demonstrates that methylammonium chloride (MACl) enhances of $FAPbI_3$ crystallization and suppresses residual lead iodide (PbI_2) formation.[34–36] Comparative XRD patterns under varied vapor conditions (**Figure 3a**; Figure S4b, Supporting Information) indicate attenuated diffraction peaks for vapor-free processed films. DMSO vapor-assisted films exhibit intensified peak signatures yet retain residual PbI_2, whereas mixed vapor-assisted (DMSO:tBP:PEA = 1000:60:1) films achieve maximal peak intensity with near-complete PbI_2,

© 2025 Wiley-VCH GmbH

16136829, 2025, 38, Downloaded from https://onlinelibrary.wiley.com/doi/10.1002/smll.202506937 by Cas-Beijing Institution Of, Wiley Online Library on [29/09/2025]. See the Terms and Conditions (https://onlinelibrary.wiley.com/terms-and-conditions) on Wiley Online Library for rules of use; OA articles are governed by the applicable Creative Commons License

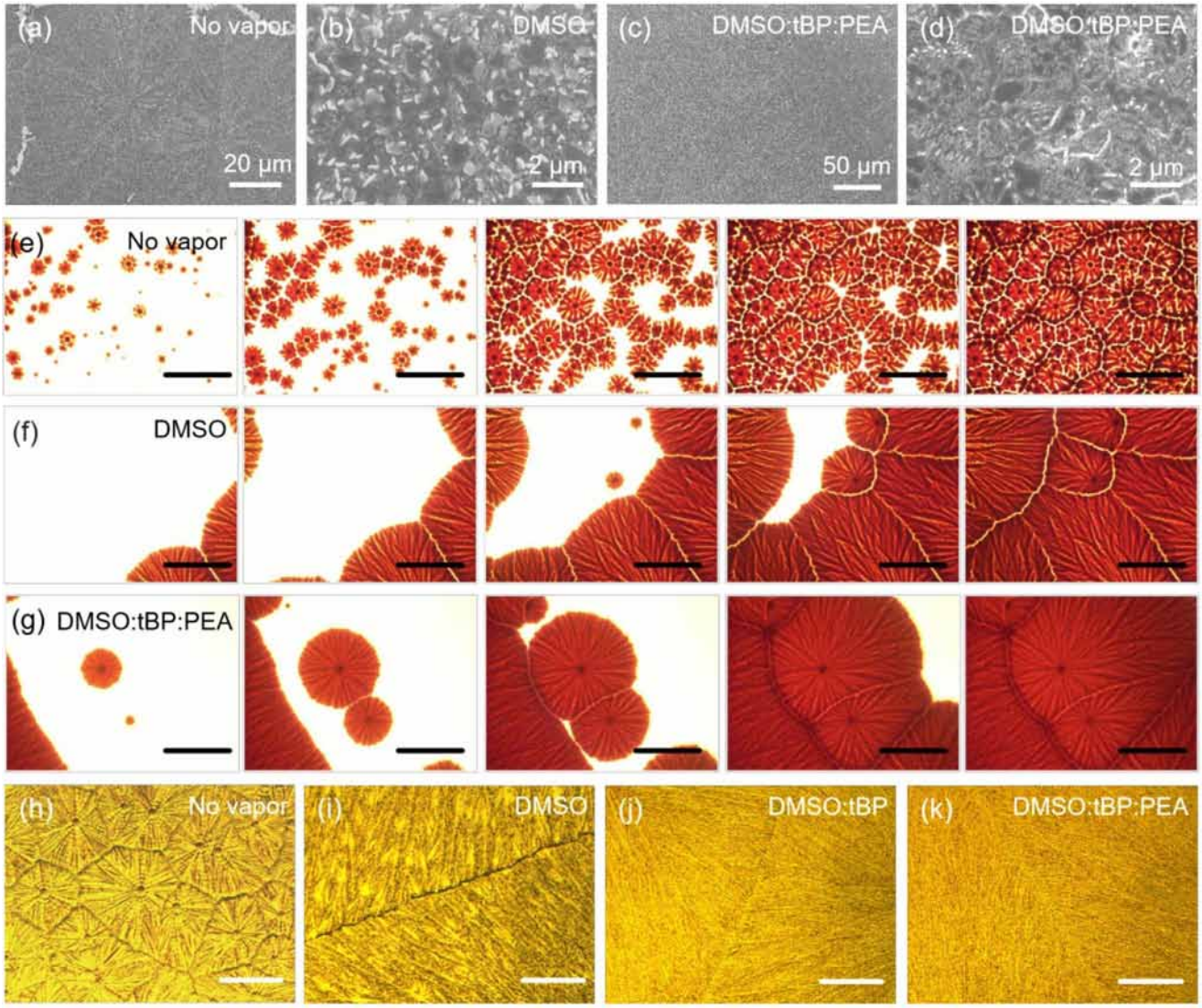

Figure 2. Morphology of perovskite films prepared in different vapors: a–d) SEM images of perovskite films made using different vapors; e–g) Optical microscopy images (transmission mode) recorded during crystallization processes of perovskite films made in different vapors (scale bar: 200 μm); h–k) Optical microscopy images (reflection mode) of perovskite films made in different vapors (scale bar: 150 μm).

confirming optimized crystallinity. Some weak peaks not belong to I-based perovskites are belong to $MAPbCl_3$ (Figure S5, Supporting Information), which forms form PbI_2 and MACl additives. Photoluminescence (PL) spectra (Figure 3b; Figure S6, Supporting Information) further demonstrate that films synthesized with the mixed vapor exhibit the highest fluorescence intensity, indicating reduced defect-state density and suppressed nonradiative recombination. This aligns with XRD findings, where MACl-enhanced $FAPbI_3$ crystallization and mixed vapor synergistically improve crystal quality. Static UV-Vis absorption spectra of films made under different vapor conditions (Figure 3c; Figure S7, Supporting Information), measured at room temperature, corroborate the enhanced absorption of mixed-vapor-processed films. To probe vapor-assisted crystallization dynamics, a custom-built in situ absorption measurement setup was employed (Figure 3d): a transparent hot plate heated the substrate within a vapor-filled quartz chamber. In situ absorption spectra of films during crystallization at 150 °C (Figure 3e,f; Figure S8, Supporting Information) reveal that vapors like DMSO moderately slow down crystallization kinetics. Time-resolved absorption at 710 nm quantifies perovskite nucleation onset delays from 5.5 s (vapor-free) to 12 s (mixed vapor) and 20 s (DMSO) (Figure 3g), with corresponding nucleation/growth durations extending from 2.5 to 3.9 and 5.8 s, respectively. Absorption spectra during the whole crystallization process (under 150 °C) show the same absorption onset (Figure 3h,i; Figure S9, Supporting Information), indicating that the precursors directly convert to perovskite phase without formation of intermediate phase. The narrower light absorption range observed under high-temperature conditions, compared to that measured at room temperature, is due to a blueshift in the absorption spectra of perovskite materials as temperature increases (Figure S10, Supporting Information). Similar

© 2025 Wiley-VCH GmbH

16136829, 2025, 38, Downloaded from https://onlinelibrary.wiley.com/doi/10.1002/smll.202506937 by Cas-Beijing Institution Of, Wiley Online Library on [29/09/2025]. See the Terms and Conditions (https://onlinelibrary.wiley.com/terms-and-conditions) on Wiley Online Library for rules of use; OA articles are governed by the applicable Creative Commons License

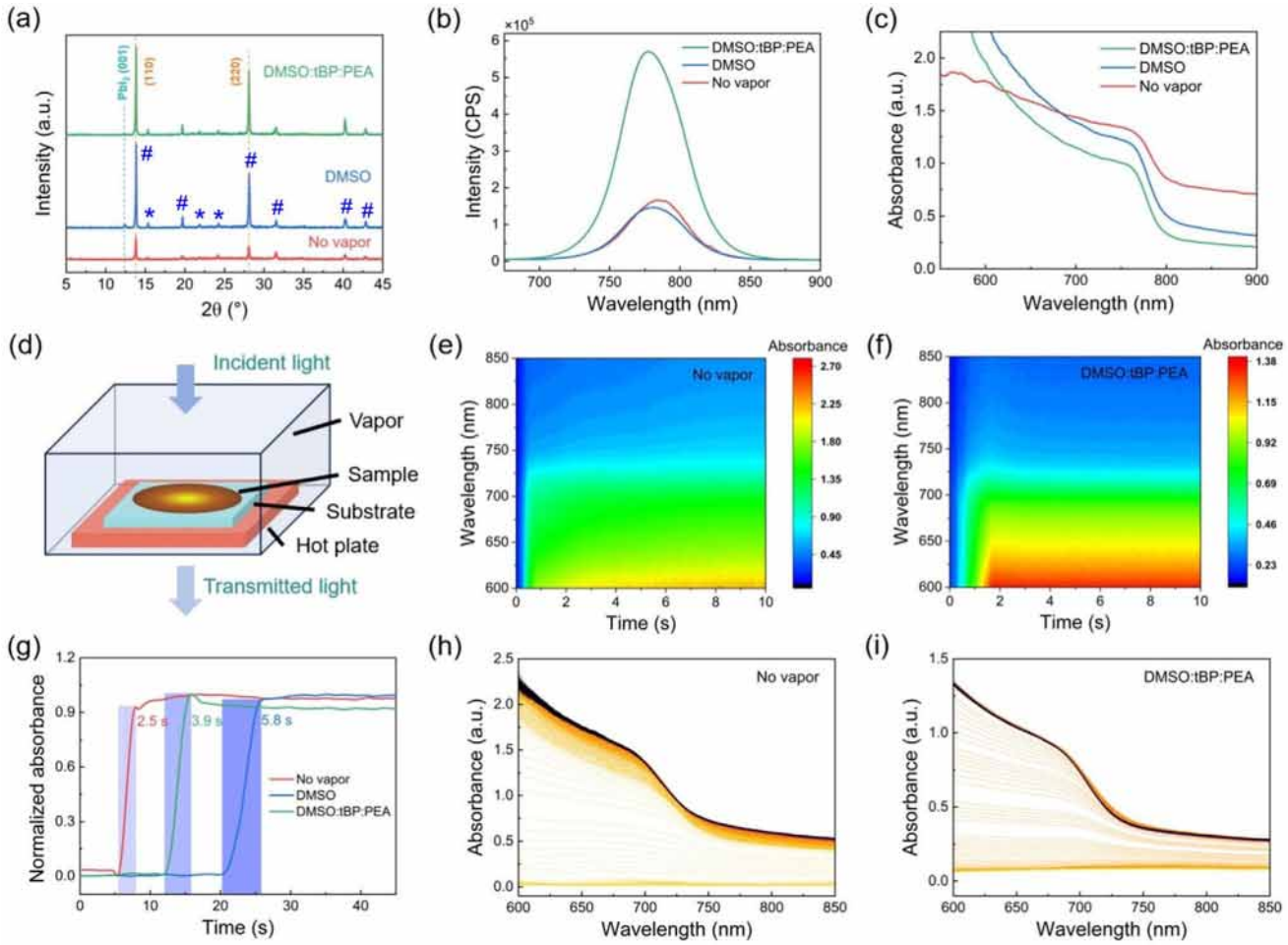

Figure 3. a) XRD patterns (# means peaks for (FAMACs)PbI_3, * means peaks for $MAPbCl_3$), b) PL spectra, and c) UV–vis absorption spectra of perovskite films made in different vapors; d) Schematic diagram of in situ absorption measurement setup during vapor-assisted crystallization of perovskite films; e,f) In situ absorption data during crystallization processes of perovskite films; g) Absorption evolution at 710 nm during the crystallization process of perovskite films prepared in different vapors; h,i) Time-dependent UV–vis absorption spectra during crystallization processes of perovskite films made in different vapors (0.07 s per spectrum).

result was also observed in other perovskite materials.[37,38] While vapors like DMSO moderately slow down crystallization, they simultaneously improve film quality, resulting in sharper absorption edge.

Spatially resolved photoluminescence (PL) intensity mapping of perovskite film made in air shows many dark spots (lower PL intensity), indicating high non-radiative recombination (**Figure** 4a). The film made in DMSO vapor shows darker grain boundary (Figure S11, Supporting Information). In contrast, the film made in DMSO:tBP:PEA vapor shows more uniform PL intensity, both at grain boundary (Figure 4b) and inside grain (Figure 4c). Fluorescence lifetime imaging microscopy (FLIM) profile of the film made without vapor show obvious lifetime difference, especially at the grain boundary (Figure 4d). In contrast, vapor-assisted films display uniform fluorescence lifetime profiles and indistinct grain boundaries (Figure 4e,f), indicative of improved uniformity, reduced defect density, and suppressed non-radiative recombination. Photothermal deflection spectroscopy (PDS) measurements (Figure S12, Supporting Information) quantify the defect-mitigating effects: DMSO vapor-processed films exhibit Eu = 18.3 ± 0.5 meV, representing a 22% reduction compared to vapor-free films (23.5 ± 0.7 meV), confirming suppressed bandtail states.

By comprehensive analysis of the morphology, crystallization, and PL data, a possible mechanism is proposed and illustrated in Figure 4g–i. As shown in Figure 4g, the commonly used antisolvent method for preparing perovskite films involves passing through an intermediate phase during crystallization, with the perovskite forming after annealing. In contrast, the hot crystallization method allows the solution to directly form perovskite during the process, while the addition of amine-based molecules enables simultaneous defect passivation in situ during crystallization. The slower crystal growth speed facilitates the ions to form ordered structure, enabling higher crystallinity, better uniformity, and more compact grain boundary. The enhanced PL intensity is due to the defect-passivation effect of tBP and PEA: nitrogen atom in the pyridine ring of tBP and the amino group of PEA interact with undercoordinated Pb^{2+} ions (Figure 4h),

© 2025 Wiley-VCH GmbH

16136829, 2025, 36, Downloaded from https://onlinelibrary.wiley.com/doi/10.1002/smll.202506937 by Cas-Beijing Institution Of, Wiley Online Library on [29/09/2025]. See the Terms and Conditions (https://onlinelibrary.wiley.com/terms-and-conditions) on Wiley Online Library for rules of use; OA articles are governed by the applicable Creative Commons License

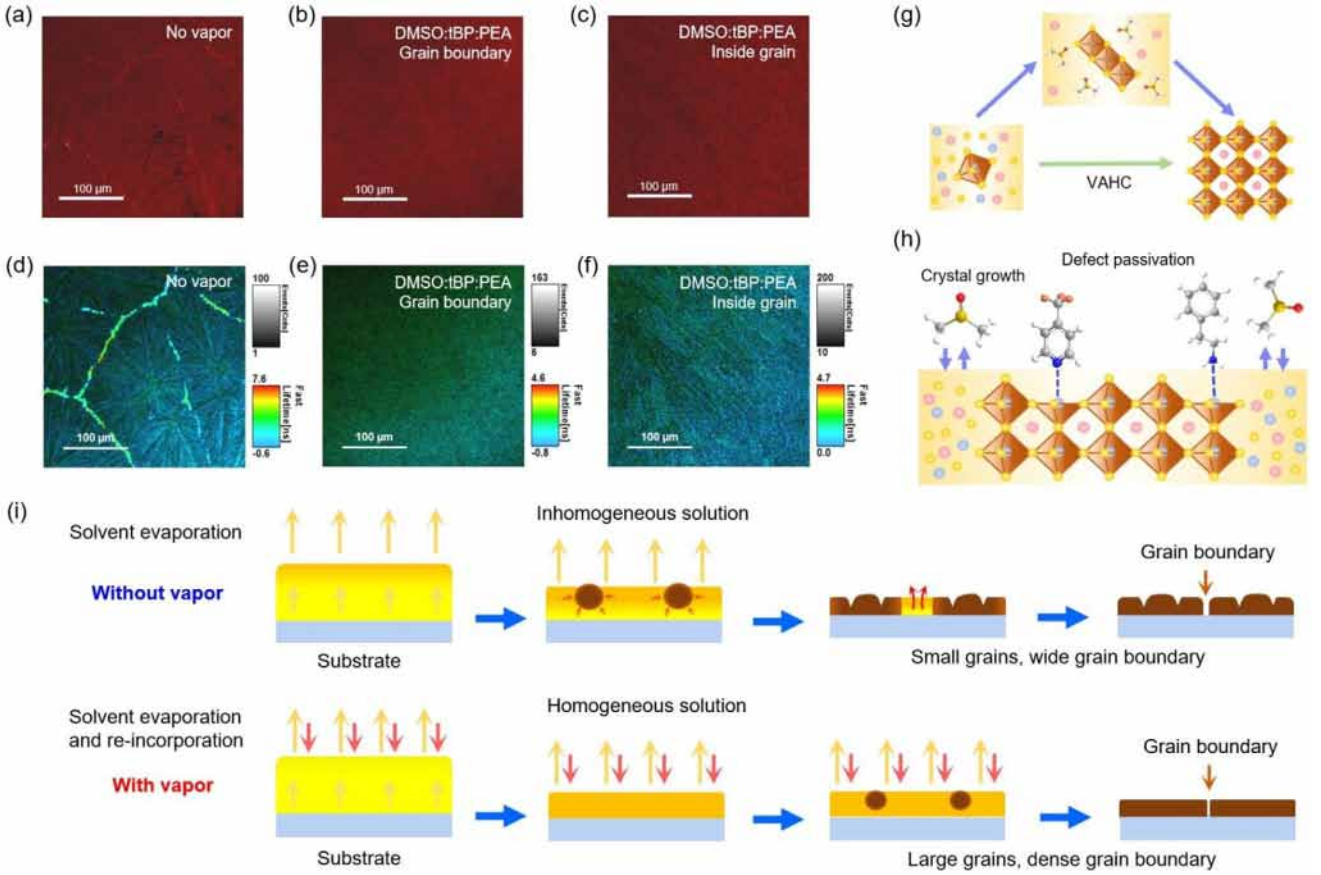

Figure 4. a–c) PL mapping of perovskite films made in different vapors; d–f) FLIM images of perovskite films made in different vapors; g) Comparison of perovskite formation pathways: conventional antisolvent method (via intermediate phase) vs. hot-crystallization method (direct formation); h) Schematic of interactions between tBP, PEA, and perovskite; i) Schematic of nucleation and crystal growth of perovskite film in air or in DMSO vapor.

effectively passivating iodine vacancy defects at surfaces/grain boundaries,[39–42] resulting in enhanced PL intensity. The vapor atmosphere plays a crucial role in both the solution flow within the wet film and the resulting grain morphology. For films fabricated without vapor, the rapid evaporation of the solvent leads to high supersaturation, a high concentration of nuclei, and accelerated crystal growth, ultimately resulting in small domains (≈200 μm). The fast evaporation at the surface induces nucleation primarily at the top layer, while the underlying solution remains unsaturated. This creates convection currents around the nuclei, leading to an undulating grain surface and wide grain boundaries (Figure 4i). In contrast, for films prepared in DMSO vapor, the vapor-liquid equilibrium significantly reduces the evaporation rate. This slower evaporation promotes a more homogeneous wet film, minimizing concentration gradients and lowering supersaturation. As a result, fewer nuclei are formed initially, followed by uniform radial growth that produces larger domains (≈3 mm) with narrower grain boundaries. The enlarged domains and reduced grain boundary widths effectively minimize defects, which not only enhances photovoltaic performance but also improves long-term device stability.

We systematically investigated photovoltaic performance of perovskite films made using different conditions by fabricating solar cells with structure of ITO/SnO_2/perovskite/spiro-OMeTAD/Ag. Initial studies focused on precursor solution composition (Figure S13, Supporting Information, with photovoltaic parameters summarized in Table S1, Supporting Information). Films derived from $FAPbI_3$ solutions containing only PbI_2 or MACl exhibited degraded quality and compromised device efficiency, with composition-dependent effects evident. However, when both PbI_2 and MACl were added, device performance is significantly enhanced. Subsequent evaluation of devices fabricated at different crystallization temperatures (**Figure 5a**, photovoltaic parameters in Table S2, Supporting Information) confirmed that 150 °C crystallization yielded the best performance. Systematic optimization of mixed vapors (Figure 5b,c; Figures S14–S17; Tables S3 and S4, Supporting Information) revealed the critical influence of PEA and tBP concentrations in DMSO, ultimately identifying an ideal solvent ratio (DMSO:tBP:PEA = 1000:60:1). Comparative performance testing of devices fabricated under different vapor conditions (Figure 5d; Table S5, Supporting Information) demonstrated that vapor-processed devices exhibited a remarkable 89.8% power conversion efficiency (PCE) enhancement (11.92% → 22.63%). Statistical analysis of PCE distributions across 39 devices (13 per vapor composition) revealed that vapor-free control devices displayed a highly variable PCE distribution with 7.58% mean efficiency, while mixed-vapor treatment yielded tightly clustered PCE (average: 22.57%) (Figure 5e;

© 2025 Wiley-VCH GmbH

16136829, 2025, 36, Downloaded from https://onlinelibrary.wiley.com/doi/10.1002/smll.202506937 by Cas-Beijing Institution Of, Wiley Online Library on [29/09/2025]. See the Terms and Conditions (https://onlinelibrary.wiley.com/terms-and-conditions) on Wiley Online Library for rules of use; OA articles are governed by the applicable Creative Commons License

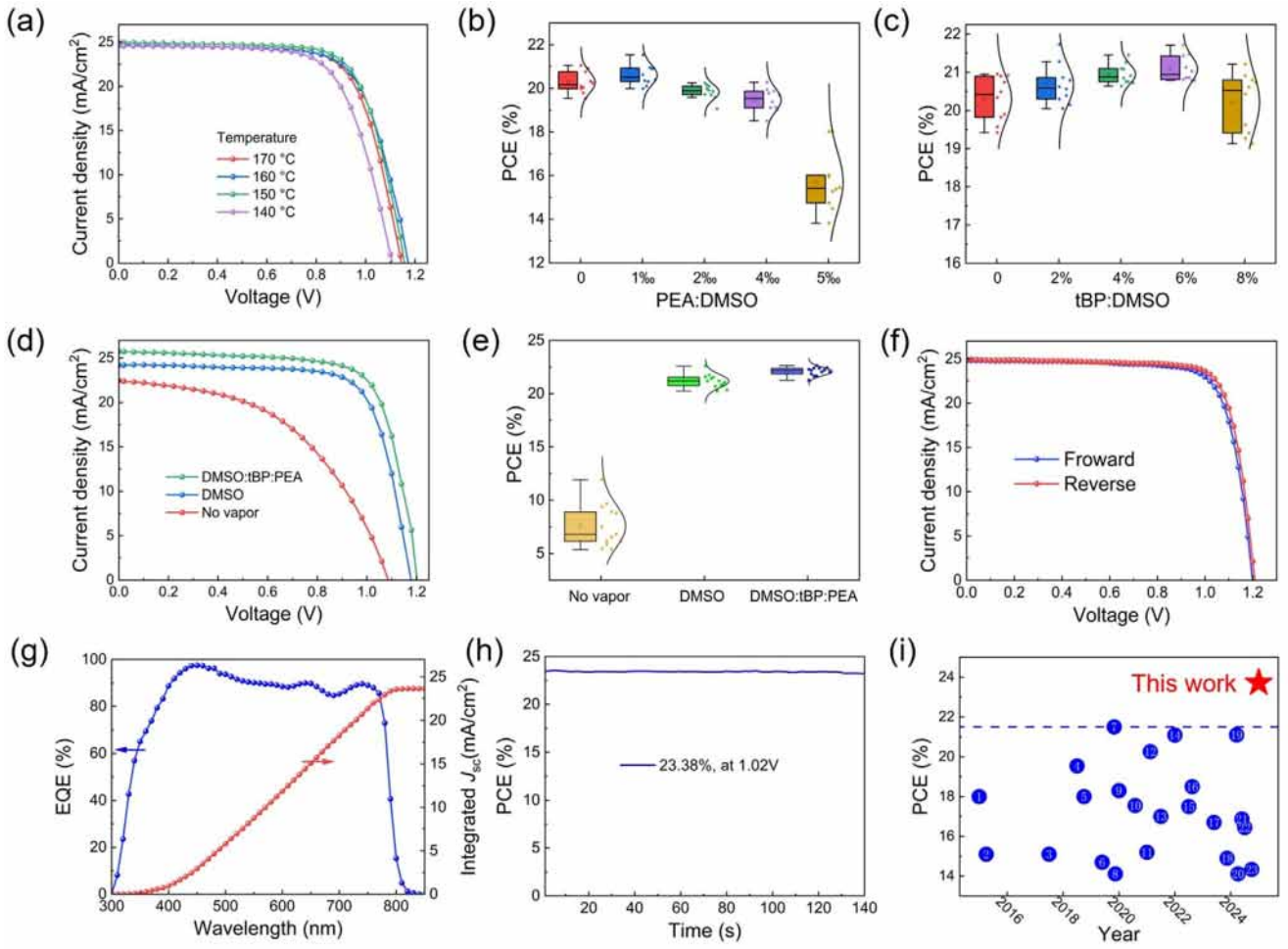

Figure 5. Performance characterization of perovskite solar cells (PSCs): a) *J–V* curves of PSCs fabricated at different temperatures; b) Statistical distribution of PCE for devices with varying PEA content in DMSO vapor; c) Statistical distribution of PCE for devices with varying tBP content in DMSO vapor; d) *J–V* curves of PSCs prepared in different vapors; e) Statistical distribution of PCE for devices under different vapor conditions; f) *J–V* curves of the champion device measured by forward and reverse scan; g) External quantum efficiency (EQE) spectrum of the champion device; h) Stabilized power output of the champion device; i) Comparison of PCE between our device and previously reported PSCs fabricated via hot-crystallization methods (numbers in circles correspond to devices listed in Table S7, Supporting Information).

Figure S19, Supporting Information). The champion device exhibited a PCE of 23.72% (Figure 5f; Table S6, Supporting Information), with an open-circuit voltage (V_{oc}) of 1.21 V, a short-circuit current density (J_{sc}) of 24.94 mA cm^{-2}, a fill factor (FF) of 78.68%, and an EQE-derived J_{sc} of 23.65 mA cm^{-2} (Figure 5g). A PCE of 22.97% is obtained by forward scan. The champion cell shows a steady-state PCE of 23.41% (Figure 5h). To our best knowledge, the PCE in this work is the highest for perovskite solar cells made using hot-crystallization method (Figure 5i; Table S7, Supporting Information). Stability testing revealed excellent durability, with unencapsulated devices retaining 96% of initial efficiency after 312 h storage in ambient air (Figure S20, Supporting Information).

3. Conclusion

In summary, a vapor-assisted hot crystallization method is developed to make perovskite films. By establishing a synergistic vapor-phase environment (DMSO:tBP:PEA = 1000:60:1), we decoupled nucleation and growth kinetics, enabling the formation of large-domain, compact, and defect-suppressed perovskite films within 30-s crystallization. The vapor-mediated process achieves three critical advancements. Reincorporation of DMSO vapor extends the nucleation and crystal growth stages, producing much larger grains and suppressing parasitic PbI_2 phases. Coordinated tBP/PEA vapors passivate interfacial defects through Pb-N and Pb-NH_2 bonding. Boundary densification eliminates light-scattering and transmission losses. The resultant solar cells achieve a PCE of 23.72%, which is the highest PCE for perovskite solar cells made using hot-crystallization method. The cells show exceptional operational stability (96% efficiency retention after 312 h ambient exposure). This vapor-phase engineering strategy needs a total heating time of <3 min, thus reducing thermal budget by >90% compared to conventional annealing (annealing time: ≈30 min), presenting a fast, low-cost, and energy-efficient pathway for manufacturing of efficient and

© 2025 Wiley-VCH GmbH

16136829, 2025, 38, Downloaded from https://onlinelibrary.wiley.com/doi/10.1002/smll.202506937 by Cas-Beijing Institution Of, Wiley Online Library on [29/09/2025]. See the Terms and Conditions (https://onlinelibrary.wiley.com/terms-and-conditions) on Wiley Online Library for rules of use; OA articles are governed by the applicable Creative Commons License

stable perovskite photovoltaics. This study demonstrates the transformative potential of vapor-assisted hot crystallization for rapid fabrication of high-performance perovskite solar cells.

Supporting Information

Supporting Information is available from the Wiley Online Library or from the author.

Acknowledgements

The authors thank the National Key Research and Development Program of China (2022YFB3803300) and the Beijing Natural Science Foundation (IS23037) for financial support.

Conflict of Interest

The authors declare no conflict of interest.

Data Availability Statement

The data that support the findings of this study are available from the corresponding author upon reasonable request.

Keywords

fast crystallization, large domain, perovskite solar cells, stability, vapor-assisted hot crystallization

Received: June 10, 2025
Revised: July 19, 2025
Published online: August 4, 2025

[1] S. Liu, J. Li, W. Xiao, R. Chen, Z. Sun, Y. Zhang, X. Lei, S. Hu, M. Kober-Czerny, J. Wang, F. Ren, Q. Zhou, H. Raza, Y. Gao, Y. Ji, S. Li, H. Li, L. Qiu, W. Huang, Y. Zhao, B. Xu, Z. Liu, H. J. Snaith, N.-G. Park, W. Chen, *Nature* **2024**, *632*, 536.
[2] W. Peng, K. Mao, F. Cai, H. Meng, Z. Zhu, T. Li, S. Yuan, Z. Xu, X. Feng, J. Xu, M. D. McGehee, J. Xu, *Science* **2023**, *379*, 683.
[3] S. Yu, Z. Xiong, H. Zhou, Q. Zhang, Z. Wang, F. Ma, Z. Qu, Y. Zhao, X. Chu, X. Zhang, J. You, *Science* **2023**, *382*, 1399.
[4] T. Bu, J. Li, H. Li, C. Tian, J. Su, G. Tong, L. K. Ono, C. Wang, Z. Lin, N. Chai, X.-L. Zhang, J. Chang, J. Lu, J. Zhong, W. Huang, Y. Qi, Y.-B. Cheng, F. Huang, *Science* **2021**, *372*, 1327.
[5] X. Li, W. Zhang, X. Guo, C. Lu, J. Wei, J. Fang, *Science* **2022**, *434*, 434.
[6] D. I. Kutsarov, E. Rezaee, J. Lambert, W. T. Stroud, A. Panagiotopoulos, S. R. P. Silva, *Adv. Mater. Technol.* **2025**, *10*, 2401834.
[7] J. Jin, Z. Zhu, Y. Ming, Y. Zhou, J. Shang, S. Wang, X. Cui, T. Guo, D. Zhang, G. Tang, Q. Lin, J. Li, X. Liu, S. Liu, Z. Chen, Z. Hu, H. Meng, Q. Tai, *Nat. Commun.* **2025**, *16*, 90.
[8] Z. Li, C. Jia, Z. Wan, J. Cao, J. Shi, J. Xue, X. Liu, H. Wu, C. Xiao, C. Li, M. Li, C. Zhang, Z. Li, *Nat. Commun.* **2025**, *16*, 1771.
[9] W. Zhang, J. Liu, W. Song, J. Shan, H. Guan, J. Zhou, Y. Meng, X. Tong, J. Zhu, M. Yang, Z. Ge, *Sci. Adv.* **2025**, *11*, adr2290.
[10] J.-E. Kim, S.-S. Kim, C. Zuo, M. Gao, D. Vak, D.-Y. Kim, *Adv. Funct. Mater.* **2019**, *29*, 1809194.
[11] Y. Y. Kim, T.-Y. Yang, R. Suhonen, A. Kemppainen, K. Hwang, N. J. Jeon, J. Seo, *Nat. Commun.* **2020**, *11*, 5146.
[12] M. Wang, C. Fei, M. A. Uddin, J. Huang, *Sci. Adv.* **2022**, *8*, abo5977.
[13] H. Min, J. Hu, Z. Xu, T. Liu, S.-U.-Z. Khan, K. Roh, Y.-L. Loo, B. P. Rand, *Adv. Mater.* **2022**, *34*, 2205309.
[14] R. Ahmad, P. J. S. Buenconsejo, M. P. A. Lim, P. C. Harikesh, V. Sugathan, R. Haselsberger, T. M. Koh, W. L. Leong, N. Mathews, A. Bruno, M.-E. Michel-Beyerle, S. G. Mhaisalkar, *Sol. RRL* **2024**, *8*, 2300746.
[15] J. J. van Franeker, K. H. Hendriks, B. J. Bruijnaers, M. W. G. M. Verhoeven, M. M. Wienk, R. A. J. Janssen, *Adv. Energy Mater.* **2017**, *7*, 1601822.
[16] C. Xue, Y. Shi, C. Zhang, Y. Lv, Y. Feng, W. Tian, S. Jin, T. Ma, *J. Power Sources* **2019**, *422*, 156.
[17] S. Du, H. Huang, Z. Lan, P. Cui, L. Li, M. Wang, S. Qu, L. Yan, C. Sun, Y. Yang, X. Wang, M. Li, *Nat. Commun.* **2024**, *15*, 5223.
[18] G. Divitini, S. Cacovich, F. Matteocci, L. Cinà, A. Di Carlo, C. Ducati, *Nat. Energy* **2016**, *1*, 15012.
[19] W. Nie, H. Tsai, R. Asadpour, J.-C. Blancon, A. J. Neukirch, G. Gupta, J. J. Crochet, M. Chhowalla, S. Tretiak, M. A. Alam, H.-L. Wang, A. D. Mohite, *Science* **2015**, *347*, 522.
[20] K.-M. Lee, C.-H. Lai, W.-C. Chu, S.-H. Chan, *Sol. Energy* **2020**, *204*, 337.
[21] J. Chen, L. Zuo, Y. Zhang, X. Lian, W. Fu, J. Yan, J. Li, G. Wu, C.-Z. Li, H. Chen, *Adv. Energy Mater.* **2018**, *8*, 1800438.
[22] Z. Bi, X. Rodríguez-Martínez, C. Aranda, E. Pascual-San-José, A. R. Goñi, M. Campoy-Quiles, X. Xu, A. Guerrero, *J. Mater. Chem. A* **2018**, *6*, 19085.
[23] M. A. Afroz, R. K. Gupta, R. Garai, M. Hossain, S. P. Tripathi, P. K. Iyer, *Org. Electron.* **2019**, *74*, 172.
[24] C. M. M. Soe, W. Nie, C. C. Stoumpos, H. Tsai, J.-C. Blancon, F. Liu, J. Even, T. J. Marks, A. D. Mohite, M. G. Kanatzidis, *Adv. Energy Mater.* **2018**, *8*, 1700979.
[25] D. Angmo, G. DeLuca, A. D. Scully, A. S. R. Chesman, A. Seeber, C. Zuo, D. Vak, U. Bach, M. Gao, *Cell Rep. Phys. Sci.* **2021**, *2*, 100293.
[26] K.-M. Lee, S.-H. Chan, M.-Y. Hou, W.-C. Chu, S.-H. Chen, S.-M. Yu, M.-C. Wu, *Chem. Eng. J.* **2021**, *405*, 126992.
[27] Y. Deng, E. Peng, Y. Shao, Z. Xiao, Q. Dong, J. Huang, *Energy Environ. Sci.* **2015**, *8*, 1544.
[28] P. You, G. Li, G. Tang, J. Cao, F. Yan, *Energy Environ. Sci.* **2020**, *13*, 1187.
[29] C. Zuo, L. Ding, *Angew. Chem., Int. Ed.* **2021**, *60*, 11242.
[30] M. Anaya, J. F. Galisteo-López, M. E. Calvo, C. López, H. Míguez, *J. Phys. Chem. C* **2016**, *120*, 3071.
[31] C. Zuo, A. D. Scully, D. Vak, W. Tan, X. Jiao, C. R. McNeill, D. Angmo, L. Ding, M. Gao, *Adv. Energy Mater.* **2019**, *9*, 1803258.
[32] L. Liu, C. Zuo, G. Liang, H. Dong, J. Chang, L. Ding, *J. Semicond.* **2024**, *45*, 010501.
[33] L. Liu, C. Zuo, L. Ding, *Nano Energy* **2021**, *90*, 106509.
[34] C. Zuo, L. Tan, H. Dong, J. Chen, F. Hao, C. Yi, L. Ding, *DeCarbon* **2023**, *2*, 100020.
[35] L. Zhang, H. Li, K. Zhang, W. Li, C. Zuo, G. O. Odunmbaku, J. Chen, C. Chen, L. Zhang, R. Li, Y. Gao, B. Xu, J. Chen, Y. Liu, Y. Wang, Y. Song, J. Tang, F. Gao, Q. Zhao, Y. Peng, M. Liu, L. Tao, Y. Li, Z. Fang, M. Cheng, K. Sun, D. Zhao, Y. Zhao, S. Yang, C. Yi, et al., *iEnergy* **2023**, *2*, 172.
[36] J. Chang, E. Feng, H. Li, Y. Ding, C. Long, Y. Gao, Y. Yang, C. Yi, Z. Zheng, J. Yang, *Nano-Micro Lett.* **2023**, *15*, 164.
[37] J. Lv, J. Wang, Y. Cheng, J. Sun, M. Lv, K. Jin, F. Long, A. Rizzo, F. Hao, K. Yan, J. Chang, C. Yi, J. Ding, Y. Ding, C. Zuo, L. Ding, *Small* **2025**, *21*, 2503214.
[38] L. Zhang, C. Zuo, M. Zhang, R. Chen, X. Chen, K. Jin, F. Hao, K. Yan, Z. Xiao, C. Wu, J. Chang, Y. Ding, L. Ding, *Angew. Chem., Int. Ed.* **2025**, *64*, 202506418.

© 2025 Wiley-VCH GmbH

16136829, 2025, 36, Downloaded from https://onlinelibrary.wiley.com/doi/10.1002/smll.202506937 by Cas-Beijing Institution Of, Wiley Online Library on [29/09/2025]. See the Terms and Conditions (https://onlinelibrary.wiley.com/terms-and-conditions) on Wiley Online Library for rules of use; OA articles are governed by the applicable Creative Commons License

[39] D. W. de Quilettes, S. M. Vorpahl, S. D. Stranks, H. Nagaoka, G. E. Eperon, M. E. Ziffer, H. J. Snaith, D. S. Ginger, *Science* **2015**, *348*, 683.
[40] K. Zou, Q. Li, J. Fan, H. Tang, L. Chen, S. Tao, T. Xu, W. Huang, *ACS Mater. Lett.* **2022**, *4*, 1101.
[41] S. Wang, A. Wang, X. Deng, L. Xie, A. Xiao, C. Li, Y. Xiang, T. Li, L. Ding, F. Hao, *J. Mater. Chem. A* **2020**, *8*, 12201.
[42] Z. Fang, J. Sun, S. F. Liu, L. Ding, *J. Semicond.* **2023**, *44*, 080201.

 © 2025 Wiley-VCH GmbH

16136829, 2025, 36, Downloaded from https://onlinelibrary.wiley.com/doi/10.1002/smll.202506937 by Cas-Beijing Institution Of, Wiley Online Library on [29/09/2025]. See the Terms and Conditions (https://onlinelibrary.wiley.com/terms-and-conditions) on Wiley Online Library for rules of use; OA articles are governed by the applicable Creative Commons License